Open Access

Catalysis Research

LIDSEN Publishing Inc.

Research Article

Iron Doped Titania/Polyaniline Composite: An Efficient Electrocatalyst for Hydrogen Evolution Reaction in Acidic Medium

Suman Lahkar, Richa Brahma, Swapan Kumar Dolui *

School of Science, Department of Chemical Science, Tezpur University, Napaam, Tezpur, India; E-Mails: sumanlahkar86@gmail.com; richabrahma6@gmail.com; dolui@tezu.ernet.in

* **Correspondence:** Swapan Kumar Dolui; E-Mail: dolui@tezu.ernet.in

Academic Editor: Diogo M. F. Santos

Special Issue: Hydrogen & Fuel Cells

Catalysis Research
2023, volume 3, issue 1
doi:10.21926/cr.2301002

Received: September 15, 2022
Accepted: December 19, 2022
Published: January 04, 2023

Abstract

The development of noble metal-free catalyst for hydrogen evolution reaction (HER) is the primary challenge in fuel production to replace fossil fuels. Here, we have synthesized Fe-doped TiO_2/PANI nanocomposite via facile in situ polymerization method and studied its electrocatalytic activity towards HER. The composite catalyzes HER efficiently with an overpotential value of -180 mV vs. RHE in 0.5 M H_2SO_4 solution to achieve the current density of 10 mA cm^{-2} and also possesses unique stability of 8 h. However, a unique balance of PANI content must be maintained to draw the maximum efficiency from the conjuncture of active Fe-doped TiO_2 particles and PANI. The catalytic efficiency of PANI is upgraded by interfacial electronic coupling with Fe-doped TiO_2, due to which the antibonding states of nitrogen atom got occupied, leading to a weaker interaction between adsorbate hydrogen and catalyst surface and enhancing the rapid desorption of H_2.

Keywords

Hydrogen evolution reaction; electrocatalyst; polyaniline nanotube; electrochemical active surface area

1. Introduction

The ever-rising global demand for energy and awareness of environmental issues related to fossil fuel drifted the research interest to search for clean and sustainable energy resources for substitution. In modern society, energy and the environment are the two key issues necessary for developing an eco-friendly world. Among the alternate fuel sources, including methanol, ethanol, propane, hydrogen, biodiesel, etc., hydrogen production has been considered the best crucial substitute for fossil fuel due to its highest possible energy density [1], sustainability, zero greenhouse gas emission property [2], and most importantly, zero by-product. But commercial hydrogen production is pioneered by fossil fuels, which is counter-productive to our cause since steam reforming of natural gas releases massive amounts of greenhouse gases into the atmosphere. A serene way to produce hydrogen gas is via electrochemical water splitting, where hydrogen gas is released by a process called the hydrogen evolution reaction (HER), promoted by an electrocatalyst [3, 4]. The efficiency of this reaction lies in its full-time operation regardless of weather conditions. For decades until now, Pt has been considered the most effective HER catalyst due to its highest cathodic current density. But less abundance and high cost of Pt halt the broad utilization preventing the commercialization of the process. Therefore, intense research activity persists in searching for cost-effective and earth-abundant non-platinum materials with low cathodic overpotential value. Non-noble metals (Ni, Co, Mo, Fe) and their metal oxides, sulfides, phosphides, and some other porous materials, including conductive metal-organic framework and other doped carbon materials, are being explored for their possibilities as cathodic electrocatalysts [5-8].

Fe is highly suitable as a cathodic electrocatalyst for the HER reaction because of its easy availability, low cost, and low toxicity. Fe^{3+} doped TiO_2 has been hydrothermally prepared by Khan et al. for photocatalytic hydrogen production using visible light [9]. The use of this Fe/TiO_2 composite electrode for HER in an alkaline medium has been reported by Danilov et al. [10]. The composite coating was synthesized by electrodeposition and is outstanding. HER activity was achieved with an overpotential of 470mV at 250 mA cm^{-2}. TiO_2 plays a dual role in increasing this catalyst's surface area and active sites. A redox couple containing TiO_2 ($TiO_2 \leftrightarrow Ti_2O_3 \leftrightarrow TiOOH$) further reinforces the catalytic activity.

The mesoporous structure of TiO_2 nanoparticles supported metal catalysts offer higher stability. Among the anatase and rutile phases of titania, the anatase phase offers a better charge carrier lifetime due to being indirect band gap material. Moreover, the pure anatase phase delivers high surface area and pore volume, leading to better reactant molecule adsorptions to carry out electrocatalytic reactions [11]. The band gap of TiO_2 can be shortened further by doping with both metallic and non-metallic elements, thus positively impacting their photocatalytic and electrocatalytic performance. Doping can also enhance metal-support interactions, leading to increased electrocatalytic properties [12, 13]. However, titania's applications are limited by its lower electrical conductivity. One of the major reasons why Fe has not been explored elaborately as an HER catalyst is that 3d transition metals are unstable in acids. However, an acidic medium is generally preferred for HER reactions [14]. This is because, in the acidic medium, the number of protons in the electrolyte is higher, leading to better facilitation of hydrogen generation.

The flaws of TiO_2 and Fe nanoparticles regarding lower electrical conductivity and corrosion in the acidic medium are conventionally overwhelmed by using nanostructured carbon materials (like graphene, amorphous carbon, and multiwalled carbon nanotubes (MWCNTs) [15]. However, the

use of Polyaniline (PANI) is not as much discussed in this aspect as the carbon-based materials, although PANI has been regarded as one of the promising candidates for electrocatalytic reactions, and supercapacitor because of its excellent chemical stability, high conductivity, strong adsorption capability of reactants, and also corrosion resistivity towards active metal elements [16, 17]. Hence, our present study synthesized a PANI-based composite for HER. But regardless of the above-mentioned unique properties of PANI, HER doesn't benefit much from PANI alone because of its ill-suited hydrogen adsorption. Recent studies have focused on, improving catalytic activity by optimizing the interfacial coupling between the support and active component to finely tune their electronic states and active sites [18, 19]. Here, we tried to increase the efficiency of PANI towards HER by interfacial electronic coupling with Fe-doped TiO_2. The composite Fe-doped TiO_2@PANI has been synthesized by a simple and green in situ polymerization method. The physical properties of the catalyst are investigated by X-ray diffraction (XRD), Fourier transforms infrared spectroscopy (FTIR), scanning electron microscopy (SEM), and transmission electron microscopy (TEM). The electrochemical performance of the electrocatalyst is evaluated by studying its polarization curve and Tafel plot. The electrostatic impedance spectroscopic (EIS) analysis technique assesses the catalyst's conductivity. The plausible mechanism of HER is also discussed.

2. Materials and Methods

2.1 Materials Used

All the chemicals including titanium tetraisopropoxide (TTIP), Iron (III) nitrate nonahydrate ($Fe(NO_3)_3{\cdot}9H_2O$), Methanol (CH_3OH), Ammonium peroxodisulfate ($(NH_4)_2S_2O_8$), Hydrogen peroxide (H_2O_2), Aniline (C_6HNH_2), Acetic acid (CH_3COOH), Nafion and Sulphuric acid (H_2SO_4) purchased from Sigma-Aldrich are of analytical reagent grade purity and were used as received.

2.2 Methods

2.2.1 Synthesis of Fe-Doped TiO_2

Fe-doped TiO_2 nanoparticles were synthesized via a simple co-precipitation method [20] similarly described by Patle *et al.* 1 M TTIP into distilled water was prepared with continuous stirring for half an hour (solution 'A'). 0.05 M ferric nitrate in distilled water with continuous stirring for half an hour (solution B). Subsequently, solution B was mixed with solution A, and the solution mixture was vigorously stirred for 2 hours. The precipitate was then filtered and washed with water several times. Thus, obtained white precipitate was mixed with 20 ml H_2O_2 to get a transparent orange solution. The solution was diluted with 10 ml of distilled water until the color changed from orange to yellow. The solution was kept for 2 days for aging. Further, the solution was filtered and washed with distilled water dried at 100˚C in the oven, and calcined at 500˚C for 6 hours.

2.2.2 Preparation of PANI

In a typical procedure, 1.82 mL of aniline [21] monomer was dissolved in a 100 mL reaction solution of 0.4 M acetic acid and 1 M methanol in 200 mL distilled water. 5.71 g ammonium persulphate was similarly dissolved to provide 100 mL solutions. The solutions of aniline and oxidant were cooled at 0-5˚C for 30 mins and then mixed rapidly into a beaker and stirred vigorously for 30

sec. The mixture was left still to react for 10 hours at 0-5°C. The dark green precipitate was filtered and washed with distilled water and dried in air for 24 hours to obtain PANI.

2.2.3 Synthesis of Fe-Doped TiO_2/PANI

In the preparation of Fe-doped TiO_2/ PANI, the reaction solution of 0.4 M acetic acid and 1 M methanol in 100 mL distilled water was prepared. 0.91 mL of aniline monomer was dissolved in a 50 mL reaction solution, and 5.71 g ammonium persulphate (APS) was similarly dissolved in another 50 mL reaction solution. In the reaction solution of aniline, 0.7 g of Fe-doped TiO_2 was added and stirred for 30 mins. The aniline and APS solutions were cooled at 0-5°C for 30 mins and then stirred vigorously for 30 sec. The mixture was left still to react for 10 hours at 0-5°C. The produced was filtered and washed with distilled water and dried in air for 24 hours to obtain Fe-doped TiO_2/PANI (0.45 wt%) nanocomposite. The process was repeated with 0.80 wt% PANI content and termed to Fe-doped TiO_2/PANI (0.80 wt%) nanocomposite.

The notations, Fe-doped TiO_2/PANI and Fe-doped TiO_2@PANI, have been used interchangeably throughout the paper. Also, Fe-doped TiO_2/PANI signifies the PANI content of 0.45 wt%.

2.3 Characterization and Measurement:

To study the effect of Fe and TiO_2 on the structure of PANI nanoparticles, XRD patterns of the samples were recorded on an X-ray diffractometer (Bruker D8-advance) in the 2θ range from (15-80)°. The samples' FTIR spectra were acquired using a Nicolet Impact-410 IR spectrometer. The surface morphologies of the sample were observed by using SEM (JSM6390LV). All the electrochemical measurements were performed on a Bio-Logic SP-150 potentiostat. The electrochemical behaviors of the samples were studied using a standard three electrodes cell compartment where Pt and Ag/AgCl were used as the counter and the reference electrodes, respectively. The working electrode was prepared by dispersing 6 mg of the synthesized electrocatalyst in 0.1 mL 0.5 wt% Nafion solution and coated onto the ~0.07 cm^2 surface area of the glassy carbon electrode (GCE, radius 1.5 mm) and then naturally dried at room temperature. 0.5 M H_2SO_4 aqueous solution was used for all the electrical measurements.

3. Results

To characterize their comparison of XRD patterns of TiO_2 and Fe-doped TiO_2 led to that after doping, there is a slight shift of the peaks towards the lower angle. Crystalline nature, the samples were examined by XRD. Hydrothermally synthesized TiO_2 nanoparticles show reflections at 2θ = 25.43°, 37.76°, 48.14°, 53.95°, 55.07°, 62.76°, 68.96°, 70.26°and 75.15° which belong to (101), (004), (200), (105), (211), (204), (116), (220) and (215) planes of titania [22], respectively in pure anatase phase, no rutile peaks are detected (Figure 1(a)). Comparison of the XRD patterns of TiO_2 and Fe-doped TiO_2 led to a slight shift of the peaks towards the lower angle. The shifting signifies the difference in the radii of the lattice and dopant atom. However, the absence of any peaks other than the anatase phase in the XRD pattern confirms successful doping. In the obtained spectra of PANI (Figure 1(b)), two prominent are observed, one at peaks 2θ = 20.4° for the (020) plane and another at 2θ = 25.6° for the (200) plane [23]. After incorporating Fe-doped TiO_2 into PANI, a prominent peak

was observed at 2θ = 25.43°. The intensity of this peak was distinguishable due to the merging of the (200) plane of PANI with the (101) plane of TiO_2.

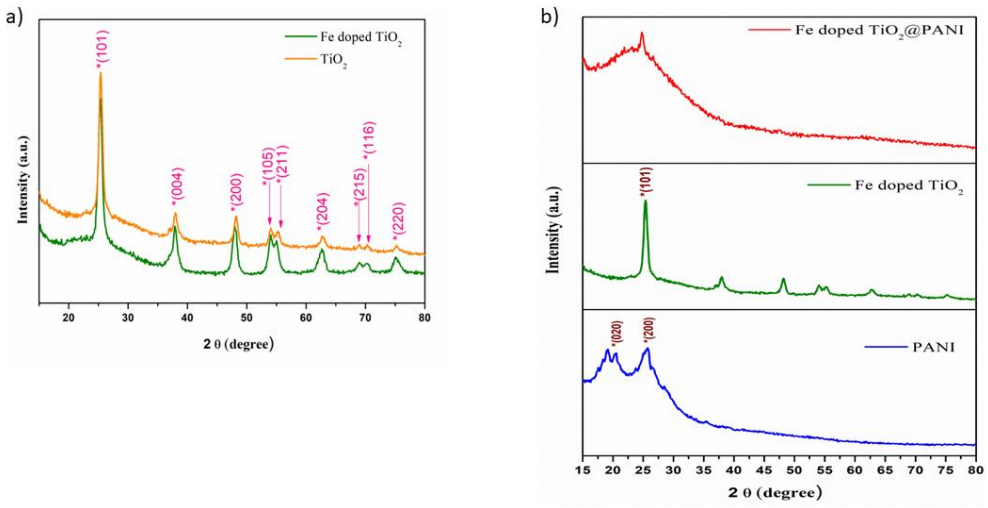

Figure 1 XRD pattern of (a) Comparison of Fe doped TiO_2 and TiO_2, (b) Fe doped TiO_2@PANI, Fe doped TiO_2 and PANI.

The FTIR spectra of pure PANI and Fe-doped TiO_2@PANI are shown in Figure 2. The broad peak at 3437 cm^{-1} for both PANI and Fe-doped TiO_2@PANI is observed to be the N-H stretching vibration of the amino group of polyanilines [24]. The peak at 2926 cm^{-1} is assigned to the C-H stretching frequency. For the C-N stretching frequency, the peak observed is at 1304 cm^{-1}, and the peak at 1572 cm^{-1} represents the benzenoid ring. The C=C vibration of the aromatic ring indicating the polymer chain was observed at the peak 1486 cm^{-1} [25-27]. The Fe-doped TiO_2/PANI spectrum shows a significant absorption peak at ~1025 cm^{-1} due to the Ti-O-C bond confirming the covalent linkage of Fe-doped TiO_2 particle to the PANI [28].

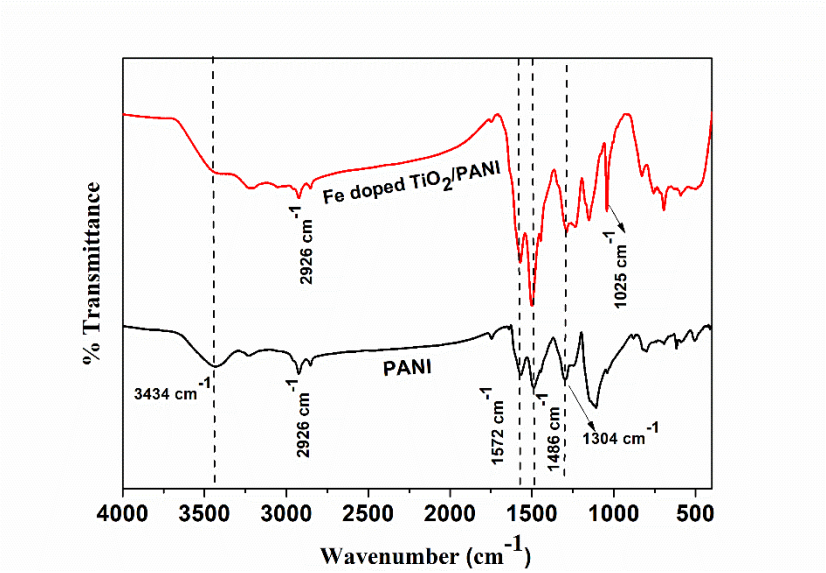

Figure 2 FTIR spectra of pure PANI and Fe doped TiO_2@PANI.

SEM image of Fe-doped TiO_2@PANI shows rough surfaces compared to that of PANI. However, no major change has been observed, implying that the major component is PANI. EDX analysis suggests the presence of C, N, O, Ti, and Fe elements in the expected ratios with negligible impurities. In Figures 3 (d) and 3 (e), the TEM images show a nearly homogeneous dispersion of metal oxide nanoparticles on PANI without any agglomeration. HRTEM image Figure 3(f) exhibits the separation of lattice fringes by 0.35 nm, which corresponds to the (002)) plane of PANI. A d spacing of 0.34 nm, corresponding to the significant (101) crystal plane of anatase phase, which is in good agreement with the p-XRD data (Figure 1(b)) and verifies that Fe doped TiO_2 particles are well supported on PANI.

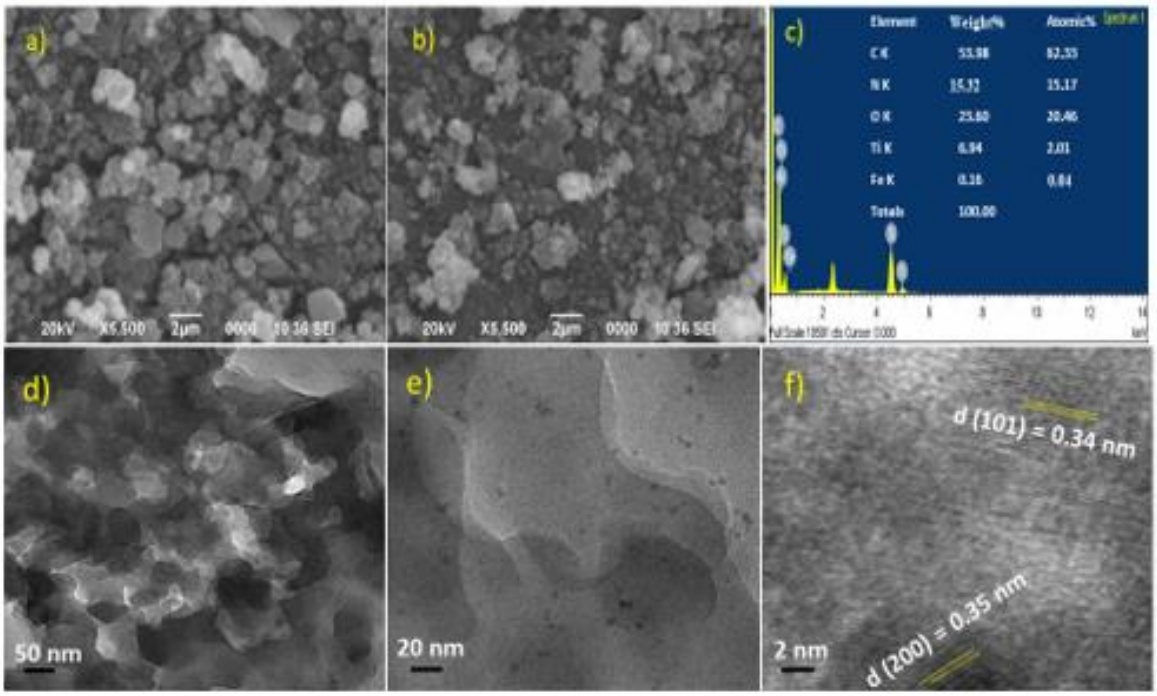

Figure 3 SEM images of (a) pure PANI, (b) Fe doped TiO_2@PANI, (c) EDX spectra of Fe doped TiO_2@PANI, (d, e) TEM images of Fe doped TiO_2@PANI at various resolutions shows distribution of Fe doped TiO_2 nanoparticles on PANI and (f) HRTEM of Fe doped TiO_2@PANI with lattice fringes corresponding to d (101) plane and d (200) planes.

The elemental valence state and the surface chemical composition of the Fe-doped TiO_2@PANI catalyst were characterized by X-ray photoelectron spectroscopy (XPS) analysis. From the high-resolution survey spectra (Figure 4a), a significant peak was observed in C 1s orbit upon fitting at 283 eV due to C-N functional group, another strong peak at 284.5eV and 285.7 eV corresponds to the C-C/C=C functional groups and oxidation developed C=O functional group. XPS spectrum of N 1s exhibited three significant peaks representing the presence of nitrogen in three different states the quinoid amine at 398.3 eV, the benzenoid amine at 399.5 eV, and the diminished nitrogen cationic radical ($N^{+\bullet}$) at 401 eV. Figure 4(c) reveals the Ti 2p spectrum split into two characteristic bands of Ti $2p_{3/2}$ and Ti $2p_{1/2}$ at the binding energy value of 458.7 eV and 464 eV, respectively reflected the presence of oxidized Ti^{4+} species [22] and the binding energy of TiO_2 was not affected by dopant concentration. O 1s spectrum shows two characteristic peaks at 529.6 eV and 531.2 eV due to the Ti-O bond and another peak at 533 eV due to several surface species, including hydroxyls,

chemisorbed oxygen [29]. In Figure 4(e), the peak observed for Fe 2p confirms the presence of Ti–O–Fe bonds due to the substitution of Ti^{4+} by Fe^{3+} [22].

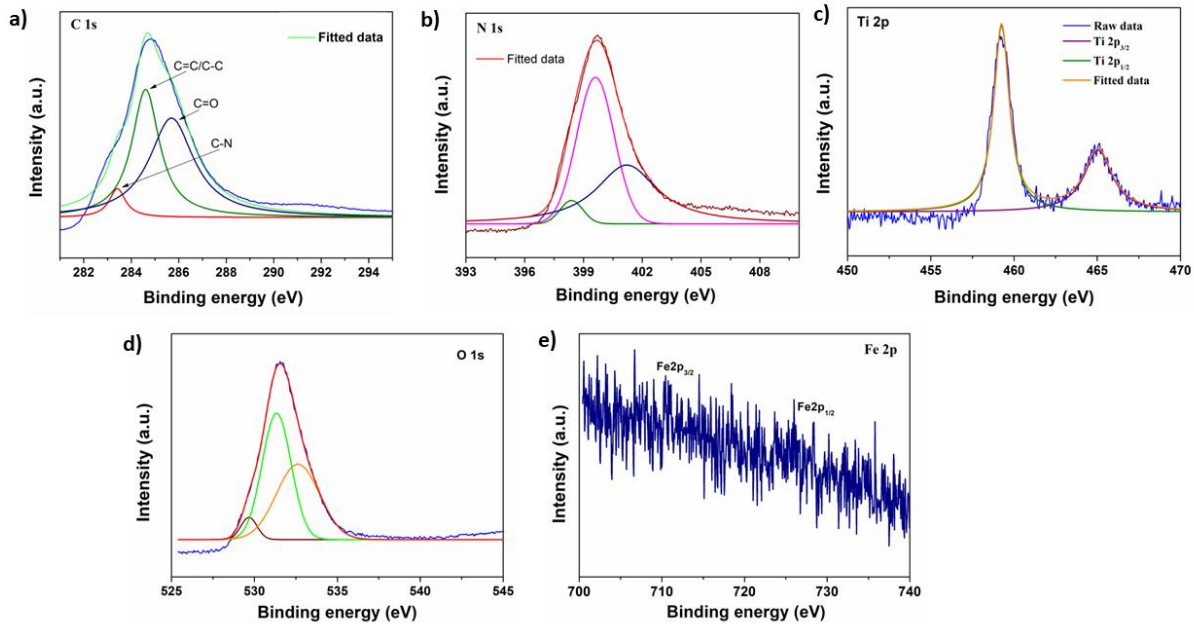

Figure 4 High resolution XPS spectra of Fe doped TiO_2@PANI a) C 1s, b) N 1s, c) Ti 2p, d) O 1s and e) Fe 2p.

4. Discussion

4.1 Electrocatalytic Activity Towards HER:

The hydrogen evolution activity of Fe-doped TiO_2@PANI composite was examined using a three-electrode set-up in 0.5 M H_2SO_4 solution at room temperature. The polarization curves (J-V plots) obtained from linear sweep voltammetry (LSV) measurements with a scan rate of 50 mV sec^{-1} were used to determine the catalytic activity. In this study, all the potentials were calibrated with a silver/silver chloride electrode (Ag/AgCl) and then converted to a reversible hydrogen electrode (RHE) using the equation E (RHE) = E(AgCl) + 0.1976 V.

From the non-zero cathodic current measurements in Figure 5(a), the onset potential for Fe-doped TiO_2@PANI with 0.45 wt% was calculated as -0.180 V, which is noticeably better than that of TiO_2@PANI (-0.207 V), Fe doped TiO_2@PANI with 0.80 wt% (-0.227 V) and PANI (-0.360 V) with same catalyst loading. It is observed that Fe-doped TiO_2@PANI with 0.45 wt% requires a relatively smaller overpotential (η_{10}) of -0.285 V vs. RHE to achieve the current benchmark density of 10 mA cm^{-2} than that of TiO_2@PANI (-0.311 V), Fe doped TiO_2@PANI with 0.80 wt% (-0.331 V) and PANI (-0.498 V). This boost comes from the strong contact of the Fe-doped TiO_2 particles with the PANI. DFT study reveals that the interplay between N sites of the PANI and metal oxides substrate leads to a favorable electronic structure that optimizes the energy for hydrogen evolution on PANI [30]. According to the Sabatier principle, a good HER catalyst's H* adsorption-free energy (ΔG_H*) is expected to have close-to-zero ΔG_H [31]. Lower ΔG_H results in very strong binding of the atomic hydrogen and hinders the desorption of H_2, while higher ΔG_H prevents the binding of atomic hydrogen on the catalyst surfaces. Thus, the reaction becomes slow unless there is a proper balance

between these two conditions. The projected density of states (DOS) study confirmed that PANI has a ΔG_H* of −1.47 eV, implying strong hydrogen adsorption on the N side of PANI [30]. Thus, the desorption of adsorbed hydrogen becomes tough, and HER kinetics turns out to be slow. But upon, the incorporation of metal oxide nanoparticles in PANI due to the electron transfer from the metal atom to the N atom of PANI leads the incoming electrons to be filled in the antibonding states of N. It thus decreases the binding energy of hydrogen with the N atom enhancing the HER kinetics. Furthermore, to examine the role of Fe doping in our catalyst, we studied the change in electronic properties of bare TiO_2 after Fe doping (Figure S2). Dopant Fe modifies the electronic structure of TiO_2 by developing new electronic states within the wide band gap of TiO_2. Thus, electrons easily reach the surface to carry out HER efficiently. The EIS analysis (Figure S2 (a)) also upholds the increased conductivity of Fe-doped TiO_2. In the case of our catalyst also, the electrons from Fe-doped TiO_2 easily reach the surface-active sites upon inducing relatively low electric potential to impel HER efficiently. However, upon increasing PANI content after 0.45 wt%, the composite efficiency towards HER was found to be decreased. This may be due to the increased PANI content covering the active sites and thus deteriorating catalytic activity.

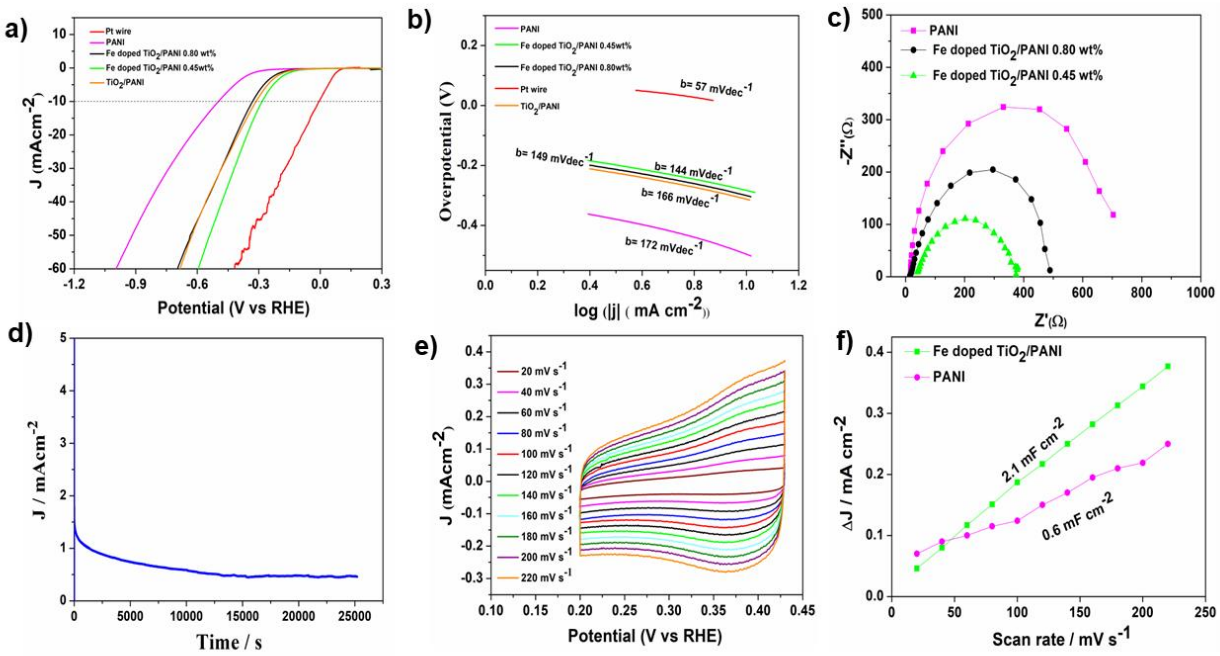

Figure 5 Electrocatalytic performance of various catalysts (a) Polarization curves showing onset potentials for HER (b) Tafel plots, (c) Nyquist plots, (d) time dependence study of the catalyst Fe doped TiO_2@PANI at an overpotential of -200 mV (Vs RHE) in 0.5 M H_2SO_4, (e) cyclic voltammograms at various scan rates from 20 mV s^{-1} to 220 mV s^{-1} within a non-faradic region, (f) variation of double layer charging current density against scan rate (C_{dl} values calculated for PANI and Fe doped TiO_2@PANI).

Tafel slopes, an inherent, intrinsic property of the catalysts analyzed the kinetics and the mechanistic pathway of HER. Fe-doped TiO_2@PANI shows a small Tafel slope value of 144 mV dec^{-1} [1] (Figure 5(b)). A smaller Tafel slope suggests a faster HER rate and a smaller energy requirement.

Electrocatalytic HER proceeds *via* two possible routes:

1) The adsorption reaction with the Tafel slope closer to 120 mV dec^{-1}, i.e., Volmer step.

$$H^+ + e^- \rightarrow H_{ads} \quad (1)$$

And

2) either of the following routes

a) The electrochemical desorption reaction (Heyrovsky step).

$$H_{ads} + H^+ + e^- \rightarrow H_2 \quad (2(a))$$

Or

b) The chemical desorption and recombination reaction (Tafel step).

$$H_{ads} + H_{ads} = H_2 \quad (2(b))$$

The combination of two of these steps, Volmer-Heyrovsky equation 1 with equation 2 (a) or Volmer-Tafel equation 1 with equation 2 (b) mechanism led to the formation of molecular hydrogen [32]. Tafel slope analysis here ensures that the HER kinetics is likely controlled by the Volmer-Heyrovsky mechanism, and releasing protons on the electrode, i.e., the Volmer step, is the rate-determining step. The plausible mechanism of HER on Fe-doped TiO_2/PANI is as follows:

$$H_3O^+(aq) + e^- + N^* \rightarrow NH_{ads} + H_2O \quad \text{(Volmer step)}$$

$$NH_{ads} + H_3O^+(aq) + e^- \rightarrow H_2(g) + H_2O(l) + N^* \quad \text{(Heyrovsky step)}$$

N* represents the active nitrogen sites of PANI and H_{ads} represents the adsorbed hydrogen.

To study the charge transfer resistance between the electrode-electrolyte interface, electrochemical impedance spectroscopy (EIS) analysis was carried out at a fixed overpotential of -270 mV vs. RHE within the frequency range from 100 MHz to 10 kHz. The charge-transfer resistance (R_{ct}) values derived from the Nyquist plots (Figure 5(c)) are 753 Ω, 469 Ω, and 335 Ω for PANI, Fe doped TiO_2@PANI (0.8 wt%), and Fe doped TiO_2@PANI (0.45 wt%) respectively. A smaller diameter suggests a quicker charge transfer process meaning better conductivity. The smaller R_{ct} value of Fe-doped TiO_2@PANI (0.45 wt%), mainly due to the efficient electron transfer from the electrode to the electrolyte, suggests the better conductivity of the catalyst validating its faster HER kinetics [33].

The durability of the catalyst was checked by performing chronoamperometric (CA) analysis for ~7 h at -200 mV (vs. RHE) overpotential (Figure 5(d)). The analysis graph fluctuated due to dehydrogenation via bubble generation and restoration of current density after the bubble detachment process. However, the catalyst maintained its integrity in catalytic efficiency towards the end. The durability test represents the applicability of the composite in HER in such an acidic environment for a long period.

Regarding the remarkable catalytic performance of Fe-doped TiO_2@PANI, the voltammetric analysis was carried out within the potential range from +0.2 V to +0.43 V with different scan rates where no faradic reaction occurred to discern the electrochemical active surface area (ECSA) (Figure 5(e)). Higher ECSA value signifies more catalytically active sites. ECSA was calculated from the electrochemical double-layer capacitance (C_{dl}) that was obtained by fitting the values of the capacitive current (i) and scanning rate (v) in equation 3.

$$i = \nu C_{dl} \quad (3)$$

C_{dl} values calculated for Fe-doped TiO_2@PANI and PANI are shown in Figure 5(f). Furthermore, the roughness factor (R_f) was calculated from the C_{dl} values, which is the ratio of the C_{dl} on 20 µF cm^{-2} (capacitive surface of a smooth electrode) [34, 35]. Calculated C_{dl}, R_f *and ECSA* values for the catalysts are given in Table 1. PANI has a specific role in the homogeneous distribution of Fe-doped TiO_2 nanoparticles and thus increases active surface sites for better HER [17]. From these values, it can be proposed that Fe-doped TiO_2@PANI has an advantage in active surface area (ECSA) and active sites over PANI to improve electrocatalytic HER activity.

Table 1 C_{dl}, R_f and ECSA values obtained for PANI and Fe doped TiO_2/PANI.

Working electrode	***C_{dl}*** **(mF cm^{-2})**	***R_f*** **(cm^{-2})**	***ECSA*** **(cm^2)**
PANI	0.6	30	2.1
Fe doped TiO_2/PANI	2.1	105	7.35

5. Conclusions

In summary, this study successfully applies environmentally friendly and cost-effective catalyst Fe doped TiO_2@PANI towards HER synthesized via a green method. The composite requires a comparatively small onset potential of 0.180 V than PANI (0.360 V). We have tried to upgrade the catalytic efficiency of PANI by interfacial electronic coupling with Fe-doped TiO_2. The efficiency improvement is solely attributed to the occupancy of the antibonding states, leading to a weaker interaction between adsorbate hydrogen and catalyst surface. However, better conductivity and improved surface area due to PANI are other factors for better catalytic performance.

Acknowledgments

The author would like to thank the Sophisticated Analytical Instrumentation Centre (SAIC), Tezpur University, India for providing analytical support.

Author Contributions

Suman Lahkar is the first author in this paper, her contributions include experimental design and operation, electrochemical measurements, and the writing of the paper. Richa Brahma helps to carry out some part of the characterization. Swapan Kumar Dolui supervises the entire work.

Competing Interests

The authors have declared that no competing interests exist.

Additional Materials

The following additional materials are uploaded at the page of this paper.

1. Figure S1: XPS survey spectra of Fe doped TiO_2@PANI.

2. Figure S2: Comparison of electrocatalytic performance of TiO_2 and Fe doped TiO_2 (a) Polarization curves showing onset potentials for HER, (b) Nyquist impedance.

References

1. Anantharaj S, Ede SR, Sakthikumar K, Karthick K, Mishra S, Kundu S, et al. Recent trends and perspectives in electrochemical water splitting with an emphasis on sulfide, selenide, and phosphide catalysts of Fe, Co, and Ni: A review. Acs Catal. 2016; 6: 8069-8097.
2. Habas SE, Platt HA, van Hest MF, Ginley DS. Low-cost inorganic solar cells: From ink to printed device. Chem Rev. 2010; 110: 6571-6594.
3. Wang M, Ye C, Xu M, Bao S. MoP nanoparticles with a P-rich outermost atomic layer embedded in N-doped porous carbon nanofibers: Self-supported electrodes for efficient hydrogen generation. Nano Res. 2018; 11: 4728-4734.
4. Niu Z, Qiu C, Jiang J, Ai L. Hierarchical CoP–FeP branched heterostructures for highly efficient electrocatalytic water splitting. ACS Sustain Chem Eng. 2018; 7: 2335-2342.
5. Peng L, Zheng X, Li L, Zhang L, Yang N, Xiong K, et al. Chimney effect of the interface in metal oxide/metal composite catalysts on the hydrogen evolution reaction. Appl Catal B. 2019; 245: 122-129.
6. Seo B, Jung GY, Sa YJ, Jeong HY, Cheon JY, Lee JH, et al. Monolayer-precision synthesis of molybdenum sulfide nanoparticles and their nanoscale size effects in the hydrogen evolution reaction. ACS Nano. 2015; 9: 3728-3739.
7. Shi Y, Zhang B. Recent advances in transition metal phosphide nanomaterials: Synthesis and applications in hydrogen evolution reaction. Chem Soc Rev. 2016; 45: 1529-1541.
8. Payra S, Challagulla S, Chakraborty C, Roy S. A hydrogen evolution reaction induced unprecedentedly rapid electrocatalytic reduction of 4-nitrophenol over ZIF-67 compare to ZIF-8. J Electroanal Chem. 2019; 853: 113545.
9. Khan MA, Woo SI, Yang OB. Hydrothermally stabilized Fe (III) doped titania active under visible light for water splitting reaction. Int J Hydrog Energy. 2008; 33: 5345-5351.
10. Danilov FI, Tsurkan AV, Vasil'Eva EA, Protsenko VS. Electrocatalytic activity of composite Fe/TiO_2 electrodeposits for hydrogen evolution reaction in alkaline solutions. Int J Hydrog Energy. 2016; 41: 7363-7372.
11. Challagulla S, Nagarjuna R, Ganesan R, Roy S. TiO_2 synthesized by various routes and its role on environmental remediation and alternate energy production. Nano Struct Nano Objects. 2017; 12: 147-156.
12. Li S, Yang H, Ren R, Ma J, Jin J, Ma J. Facile fabrication of palladium-ionic liquids-nitrogen-doped graphene nanocomposites as enhanced electro-catalyst for ethanol oxidation. J Power Sources. 2015; 294: 360-368.
13. Román-Martínez MC, Cazorla-Amorós D, Linares-Solano A, Salinas-Martí'nez De Lecea C, Yamashita H, Anpo M. Metal-support interaction in Pt/C catalysts. Influence of the support surface chemistry and the metal precursor. Carbon. 1995; 33: 3-13.
14. Yu J, Jing H, Wu Z, Liu B, Lei W, Hao Q. 3D Fe_3O_4-decorated nitrogen-doped graphene aerogel as a highly durable electrocatalyst for oxygen reduction reactions. Catal Res. 2022; 2: 016.

15. Deng J, Ren P, Deng D, Yu L, Yang F, Bao X. Highly active and durable non-precious-metal catalysts encapsulated in carbon nanotubes for hydrogen evolution reaction. Energy Environ Sci. 2014; 7: 1919-1923.
16. Chen S, Wei Z, Qi X, Dong L, Guo YG, Wan L, et al. Nanostructured polyaniline-decorated Pt/C@PANI core–Shell catalyst with enhanced durability and activity. J Am Chem Soc. 2012; 134: 13252-13255.
17. Roy S, Payra S, Challagulla S, Arora R, Roy S, Chakraborty C, et al. Enhanced photoinduced electrocatalytic oxidation of methanol using Pt nanoparticle-decorated TiO_2–Polyaniline ternary nanofibers. ACS Omega. 2018; 3: 17778-17788.
18. Voiry D, Fullon R, Yang J, de Carvalho Castro e Silva C, Kappera R, Bozkurt I, et al. The role of electronic coupling between substrate and 2D MoS_2 nanosheets in electrocatalytic production of hydrogen. Nat Mater. 2016; 15: 1003-1009.
19. Deng J, Deng D, Bao X. Robust catalysis on 2D materials encapsulating metals: Concept, application, and perspective. Adv Mater. 2017; 29: 1606967.
20. Patle LB, Labhane PK, Huse VR, Gaikwad KD, Chaudhari AL. Synthesis and structural analysis of Fe doped TiO_2 nanoparticles using Williamson Hall and Scherer Model. Proceedings of the 2nd International Conference on Condensed Matter and Applied Physics (ICC 2017); 2018 May 8; Bikaner, RAJ, India. Melville: AIP Publishing LLC.
21. Huang Z, Liu E, Shen H, Xiang X, Tian Y, Xiao C, et al. Preparation of polyaniline nanotubes by a template-free self-assembly method. Mater Lett. 2011; 65: 2015-2018.
22. Koli VB, Delekar SD, Pawar SH. Photoinactivation of bacteria by using Fe-doped TiO_2-MWCNTs nanocomposites. J Mater Sci Mater Med. 2016; 27: 177.
23. Zhang Y, Liu J, Zhang Y, Liu J, Duan Y. Facile synthesis of hierarchical nanocomposites of aligned polyaniline nanorods on reduced graphene oxide nanosheets for microwave absorbing materials. RSC Adv. 2017; 7: 54031-54038.
24. Butoi B, Groza A, Dinca P, Balan A, Barna V. Morphological and structural analysis of polyaniline and poly (o-anisidine) layers generated in a DC glow discharge plasma by using an oblique angle electrode deposition configuration. Polymers. 2017; 9: 732.
25. Jarad AN, Ibrahim K, Ahmed NM. Synthesis and characterization thin films of conductive polymer (PANI) for optoelectronic device application. Proceedings of the International Conference on Nano-electronic Technology Devices and Materials 2015; 2016 July 6; Jeju, Korea. Melville: AIP Publishing LLC.
26. Tamirisa PA, Liddell KC, Pedrow PD, Osman MA. Pulsed-plasma-polymerized aniline thin films. J Appl Polym Sci. 2004; 93: 1317-1325.
27. Ohsaka T, Ohnuki Y, Oyama N, Katagiri G, Kamisako K. IR absorption spectroscopic identification of electroactive and electroinactive polyaniline films prepared by the electrochemical polymerization of aniline. J Electroanal Chem Interfacial Electrochem. 1984; 161: 399-405.
28. Singh T, Pal DB, Bhatiya AK, Mishra PK, Hashem A, Alqarawi AA, et al. Integrated process approach for degradation of p-cresol pollutant under photocatalytic reactor using activated carbon/TiO_2 nanocomposite: Application in wastewater treatment. Environ Sci Pollut Res. 2022; 29: 61811-61820.
29. Ahuja P, Ujjain SK, Arora I, Samim M. Hierarchically grown NiO-decorated polyaniline-reduced graphene oxide composite for ultrafast sunlight-driven photocatalysis. ACS Omega. 2018; 3: 7846-7855.

30. Huang ZF, Song J, Du Y, Dou S, Sun L, Chen W, et al. Optimizing interfacial electronic coupling with metal oxide to activate inert polyaniline for superior electrocatalytic hydrogen generation. Carbon Energy. 2019; 1: 77-84.
31. Ji X, Wang K, Zhang Y, Sun H, Zhang Y, Ma T, et al. MoC based Mott–Schottky electrocatalyst for boosting the hydrogen evolution reaction performance. Sustain Energy Fuels. 2020; 4: 407-416.
32. Zhu J, Hu L, Zhao P, Lee LY, Wong KY. Recent advances in electrocatalytic hydrogen evolution using nanoparticles. Chem Rev. 2019; 120: 851-918.
33. Zhang X, Jia F, Song S. Recent advances in structural engineering of molybdenum disulfide for electrocatalytic hydrogen evolution reaction. Chem Eng J. 2021; 405: 127013.
34. Fang M, Gao W, Dong G, Xia Z, Yip S, Qin Y, et al. Hierarchical NiMo-based 3D electrocatalysts for highly-efficient hydrogen evolution in alkaline conditions. Nano Energy. 2016; 27: 247-254.
35. Gao D, Guo J, Cui X, Yang L, Yang Y, He H, et al. Three-dimensional dendritic structures of NiCoMo as efficient electrocatalysts for the hydrogen evolution reaction. ACS Appl Mater Interfaces. 2017; 9: 22420-22431.